Extreme ultraviolet mask substrate surface roughness effects on lithographic patterning

Simi A. George,[a] Patrick P. Naulleau,[b] Iacopo Mochi, Farhad Salmassi, Eric M. Gullikson, Kenneth A. Goldberg, and Erik H. Anderson
Center for X-Ray Optics, Lawrence Berkeley National Laboratory, 1 Cyclotron Road, Berkeley, California 94720

In extreme ultraviolet lithography exposure systems, mask substrate roughness-induced scatter contributes to line edge roughness (LER) at the image plane. In this article, the impact of mask substrate roughness on image plane speckle is explicitly evaluated. A programed roughness mask was used to study the correlation between mask roughness metrics and wafer plane aerial image inspection. The authors find that the roughness measurements by the top surface topography profile do not provide complete information on the scatter related speckle that leads to LER at the image plane. They suggest at-wavelength characterization by imaging and/or scatter measurements into different frequencies as an alternative for a more comprehensive metrology of the mask substrate/multilayer roughness effects. © *2010 American Vacuum Society.* [DOI: 10.1116/1.3502436]

I. INTRODUCTION

Extreme ultraviolet lithography (EUVL)[1–3] remains the top candidate for high volume manufacturing at a 16 nm half-pitch node. EUV based optical projection systems utilize a patterning wavelength near 13.5 nm. Wavelengths in this region are absorbing in matter; thus, an all reflective system in vacuum is a requirement. In order to achieve high reflectivities at this illuminating wavelength, the optics and the reflective photomask[4] exploit thin film interference properties with alternating thin layers of molybdenum and silicon deposited on a substrate. Further details on the theory, on the architecture and the choice of materials for the mask and optics, and on the surface fabrication processes can be found in literature.[2–6]

A considerable problem for the mask and the optics at this illuminating wavelength is roughness-induced multilayer scattering or nonspecular scattering.[5,7,8] It is well known that nonspecular scattering leads to throughput loss in the optical systems and to reduced image contrast. Multilayer scattering, which is considered to be fundamentally different from single surface scattering, is characterized by interference effects arising from the roughness of the different material interfaces as well as the conformal growth of the substrate roughness to the top layer surface. These interference effects, occurring at higher frequencies (hence treated as a statistical effect), cause phase modulations in the image field (speckle) that ultimately leads to the loss of imaging fidelity.[9] More specifically, the mask substrate roughness directly leads to line edge roughness (LER) through the formation of speckle in the patterned image.[10]

The recently updated International Technology Roadmap for Semiconductors (ITRS)[11] sets the limit LER in resists[12,13] to be less than 1.2 nm (3σ LER) at the 20 nm half-pitch resolution. Under such constraints, it has recently been shown that mask contributors to LER play a significant role.[13–16] Of particular concern is the substrate roughness issue discussed above, especially as the illumination coherence is increased.[17–19]

Modeling has shown that the mask multilayer replicated top surface roughness (RSR) must be limited to 50 pm to meet current LER targets for the 22 and 16 nm half-pitch lithography nodes.[19,20] For EUV, the phase coherent roughness that propagates from layer to layer is considered to be significant, bringing into question the suitability of top surface roughness analysis methods such as atomic force microscopy (AFM) for its characterization. Because the root cause of LER from phase coherent roughness is speckle in the aerial image, it is crucial to understand the relationships between bottom (substrate) surface roughness, top surface roughness, EUV scattering, and aerial image speckle for developing accurate mask specifications and suitable roughness metrics.

In this article, we explicitly study the impact of substrate roughness on image plane speckle. We quantify the extent to which an AFM measurement can be depended upon for specifying tolerable roughness limits on EUV masks and propose an alternative metrology method capable of directly measuring phase coherent roughness. The design of the study involved a mask prepared with areas of varying roughness that was then coated with a Mo–Si multilayer. AFM based topography was collected for each area before and after multilayer deposition. The same rough areas were then subjected to EUV reflectometry and scattering measurements to obtain phase coherent roughness parameters. These areas were then imaged at wavelength,[21] thus directly characterizing the aerial image speckle. Finally, modeling is used to test the effectiveness of the two different roughness metrologies in predicting the measured aerial image speckle.

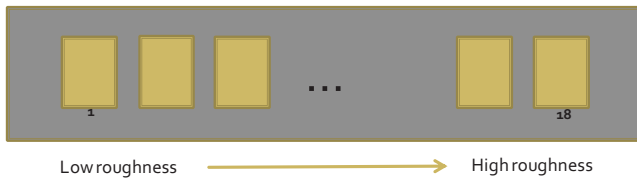[a]Electronic mail: sageorge@lbl.gov
[b]Electronic mail: pnaulleau@lbl.gov

FIG. 1. (Color online) Row of eighteen windows, sized 1×3 mm^2 and separated by 1.5 mm, patterned on a gradient of low to a high roughness region were evaluated for this study. The clear multilayer surface is inside the window, and resist absorber giving full attenuation of EUV is outside. The lowest roughness content is in window 1 and the highest roughness content is in window 18.

II. MASK MULTILAYER SURFACE CHARACTERIZATIONS

The basic structure of EUV masks starts with a highly polished quartz type substrate of low thermal expansion. Forty or more alternating layers of molybdenum (Mo) and silicon (Si) are deposited on top of the substrate to provide high EUV reflectivity. A protective capping layer is deposited on top of the multilayer, and lithographic patterning is completed with a buffer/absorber stack deposited on top of the capping layer.

A. Mask fabrication for controlled roughness studies

Since mask blanks with roughness gradients are not readily available, a masklike surface was fabricated for the measurements completed here. The fabrication procedure involved the shadowed deposition of chromium (Cr) onto a standard 4 in. silicon (Si) wafer by dc magnetron sputtering in an argon gas environment. The shadowing was controlled in such a way that a thickness gradient from 0.2 to 1.4 nm was achieved along one direction on the wafer. Since surface roughness is a function of film thickness, roughness gradients of 0.25–0.75 nm root mean squared (rms) roughness was achieved as measured by AFM.

A typical EUV molybdenum (Mo) and Si multilayer (40 alternating pairs of Si and Mo films such that each pair is 7 nm in thickness totaling approximately 240 nm) designed for near-normal reflection were deposited on top of the sputter coated Cr surface of the wafer. Peak reflectivity for this multilayer was measured to be at 13.46 nm. Instead of a real tantalum (Ta) based absorber that is typical of an EUV mask pattern, an e-beam resist is used as the absorber, which was spun coated onto the multilayer surface with thicknesses of about 380 and 760 nm round trip for full attenuation of EUV light. A grid pattern of windows sized 1×3 mm^2 and separated by 1.5 mm was exposed and developed to expose the multilayer surface. A second set of AFM images was collected from the exposed multilayer surface at roughly the same coordinates as before. For the metrologies completed here, we look at a row of 18 windows going from low roughness to high roughness, as shown in Fig. 1.

TABLE I. Roughness (root mean square deviations) computed from AFM imaged surface profiles before and after the multilayer depositions. The uncertainty in the AFM measurements for the scan area is approximated to be in the range of $\pm 10\%$ for these values given.

Window number	Chrome surface (nm rms)	Chrome surface with multilayer (nm rms)
6	0.23	0.2
7	0.3	0.27
8	0.47	0.32
10	0.59	0.43
11	0.57	0.45
12	0.63	0.47
13	0.6	0.46
14	0.68	0.48
15	0.8	0.49
16	0.73	0.52
18	0.68	0.54

B. Surface analysis by atomic force microscopy

AFM imaging of the Cr coated surface was completed at specific coordinates along the axis of increasing roughness on the wafer. After the multilayer deposition on top of the sputter coated Cr surface and grid patterning with resist, a second set of AFM images was collected from the exposed multilayer areas/windows at roughly the same coordinates as before. The instrument used for measurements is the Digital Instruments model DM 3100 scanning probe microscope developed by the Veeco metrology group. All AFM scans were completed with the Nanoscope IIIa controller over a 5 $\times 5$ μm^2 area, in the tapping mode, and analyzed offline with the commercially available image analysis package SUMMIT (Ref. 22) to determine the rms deviation roughness of the surfaces.

From the surface height distributions in the AFM surface profiles, the rms roughness is determined for the exposed multilayer windows with varying roughness content. The rms numbers tabulated for images collected before and after the Mo/Si multilayer (ML) is deposited on chrome are given in Table I. The measurements from windows 1–5 are omitted from comparisons here because of the high noise content resulting from AFM tip related artifacts observed in the scanned AFM images before the deposition of the multilayer. After ML deposition, the minimum in the measured roughness is 0.2 nm for windows 1–6, which gives approximately 1.9 nm peak-valley (p-v) errors. We note that, presently, the best EUV mask blank roughness is characterized to be near or better than 0.2 nm rms. The maximum in the roughness is found to be at 0.54 nm and corresponds to nearly 5 nm of p-v errors. We also find that the characteristic correlation lengths computed from the autocorrelation of the image surface heights are approximately 60 nm on average for the ML coated areas being analyzed here.

The tabulated rms values are plotted in Fig. 2 as a function of increasing region number (correlated with the increase in the chromium thickness and roughness). It is immediately obvious from the plot that there is roughness
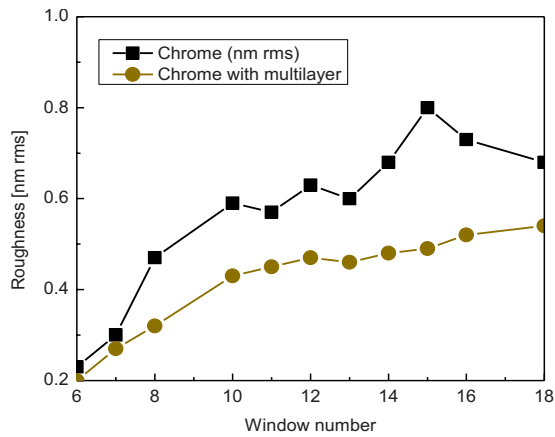
FIG. 2. (Color online) Root mean square height deviations from the AFM surface profiles of the sputter coated chrome on Si rough mask before and after Mo/Si multilayer coating. Rougher areas of the mask show smoothing after multilayer is deposited, and at smaller roughness scales, the smoothing appears to be diminished.

smoothing occurring in the rougher mask areas after the ML deposition. On the other hand, very little smoothing is observed at the smaller substrate roughness regions near 0.2 nm. We conclude that this is due to the ML itself having intrinsic roughness, and when the starting substrate roughness is too small, the smoothing effect is apparently mitigated. However, it is not clear presently how the replicated surface roughness might be affected.

To better illustrate the smoothing, the isotropic power spectral densities (PSDs) obtained for the images before and after the ML coating are compared at a roughness minimum and roughness maximum. Figure 3 shows two AFM surface measurements, specifically for mask multilayer surfaces in regions 6 and 15. The measured roughness for region 6 is 0.23 nm before ML coating and 0.2 nm after, and the surface in region 15 shows a reduction from 0.8 to 0.5 nm rms roughness after ML. In looking at the PSDs generated (Fig. 3, top) for region 6 in the low roughness region, where the solid black curve is the PSD of the chromium surface by itself, we observe an increase in the low spatial frequency range (LSFR) and some smoothing in the mid to high spatial frequencies (MSFR and HSFR) after the ML is coated. In contrast, the PSDs for region 15 (Fig. 3, bottom) with taller phase structures show significant reduction into all frequencies after ML deposition. This effect is due to the smoothing induced by the ML structures. Figure 4 shows two masks (low and high roughness components) synthesized from AFM image scans to be used for the thin mask model used for predicting phase coherent roughness contributed speckle. The phase is depicted in grayscale, and the phase errors are included from the PSD.

C. X-ray reflectance measurements

Another way to extract roughness from a surface is by using x-ray reflectance and scattering (XRS) measurements at wavelength. For this purpose, we utilized a synchrotron based reflectometer located at the advanced light source
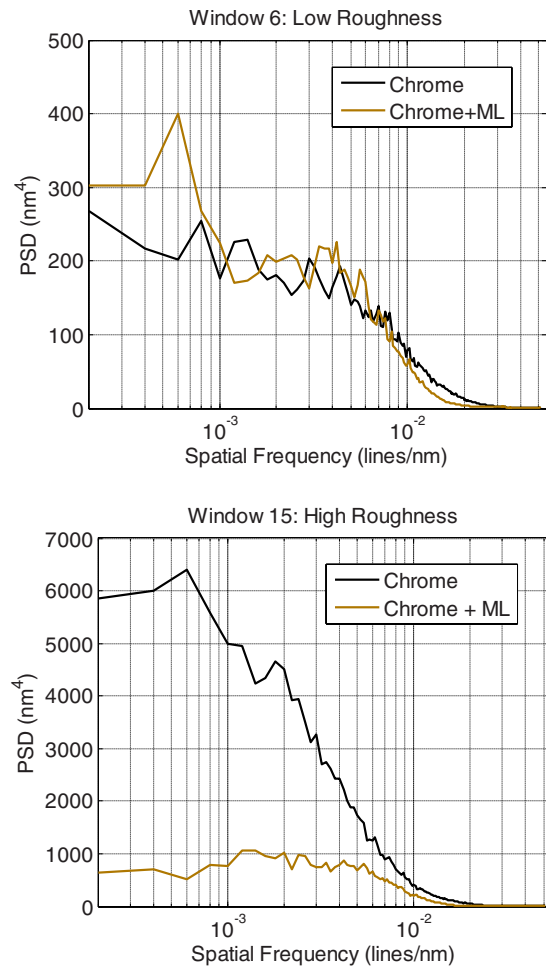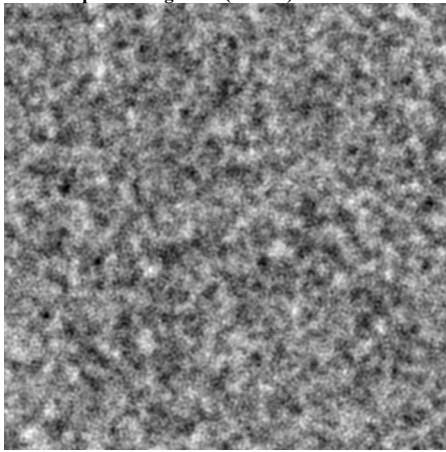

FIG. 3. (Color online) PSDs generated (window 6, top) in the low roughness region with the solid black curve are the PSDs of the chromium surface by itself. An increase in the LSFR and some smoothing into the MSFR to HSFR are observed after the ML is coated on this surface. In contrast, the PSDs for high roughness (window 15, bottom) show significant reduction into all frequencies after ML deposition. The taller phase structures are assumed to have been smoothed.

beamline 6.3.2 of the Lawrence Berkeley National Laboratory (LBNL). The main advantage of the beamline is its high spectral purity, a spectral resolving power (eV/ΔeV) of up to 7000, a wavelength accuracy of 10^{-3} nm, and a reflectivity accuracy of 0.1% (absolute). The high spectral resolution is achieved by utilizing a variable line space grating. Further details of the beamline and the instrument can be found in the literature.[23]

Reflectance measurements were performed at a wavelength of 13.46 nm with a relative spectral bandwidth, $\Delta\lambda/\lambda$, of approximately 0.01%. The photon beam is incident on the sample surface at a 5° angle from the normal, and the specular reflectance is measured at the same angle. The specular beam divergence is ±1.2°, and the detector is large in comparison to the reflected beam numerical aperture (NA). The diffuse scattering from the surfaces is measured at a fixed 5° angle from the reflected beam or 10° away from the surface normal. The raw reflectivity and scattering yields for the measurements from the different windows are shown in Fig.

A. Small phase roughness (0.2 nm)

B. High phase roughness (0.5 nm)
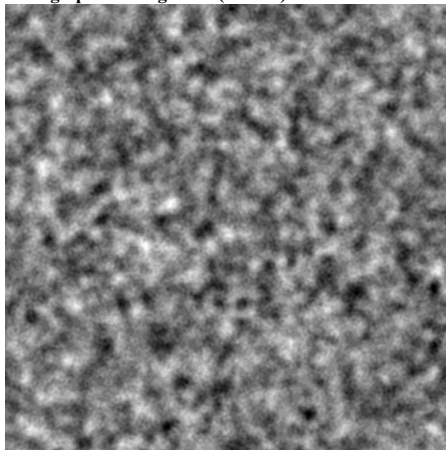
FIG. 4. Images synthesized from AFM image scans to be used for the thin mask model for predicting phase coherent roughness contributed speckle.

TABLE II. RMS roughness computed from AFM imaging and the roughness calculated from the measured XRS reflectivity of the rough mask windows.

Window number	XRS roughness (nm rms)	AFM roughness (nm rms)
6	0.10	0.2
7	0.13	0.27
8	0.23	0.32
9	0.30	n/a
10	0.36	0.43
11	0.41	0.45
12	0.44	0.47
13	0.46	0.46
14	0.48	0.48
15	0.49	0.49
16	0.50	0.52
17	0.51	n/a
18	0.52	0.54

5 on the scale of increasing roughness. Scattering measurements are obtained at a single frequency and serves to illustrate that an increase in phase roughness scatters intensity away from reflected specular beam. In Fig. 5, the increase in scattering is seen to follow the decrease in reflectivity owing to the increase in phase roughness of the measured surfaces.

In order to extract rms surface roughness from the measured reflectivities, we take advantage of the relationship between scattering and reflectivity. Assuming that reflectivity is spread over the width of the interface and assuming that this width is related to the roughness of the interface, it can be represented statistically as a Gaussian. Total reflectivity is reduced because amplitudes reflected from different depths add with different phases. For an initial reflectivity less than 1 and assuming that refraction effects are negligible, the Gaussian can be Fourier transformed from coordinates to momentum transfer to obtain reflectivity reduction as a function of wavelength or angle of incidence. The momentum transfer is replaced with the multilayer period, which leads to the Debye–Waller factor for the reduction of reflectivities to which the expression for the total integrated scatter (TIS) can be related to approximate the rms phase roughness term as follows:

$$\text{TIS} = \left(\frac{4\pi\sigma \cos \theta}{\lambda} \right)^2 = 1 - \frac{R}{R_0},$$

where σ is the rms phase roughness and λ is the illuminating wavelength at the given angle of incidence, θ. R_0 and R denote the reflectivity of the best surface and the reflectivity of the surfaces with increasing roughness content, respectively. When the roughness correlation length is large compared to the illuminating wavelength, most of the scattering will be into a small cone about the specular direction and can be related to the reflected amplitude loss. Phase roughnesses computed using this relationship and the measured reflectivities from the mask surface are tabulated in Table II, alongside the corresponding AFM measured rms roughness.
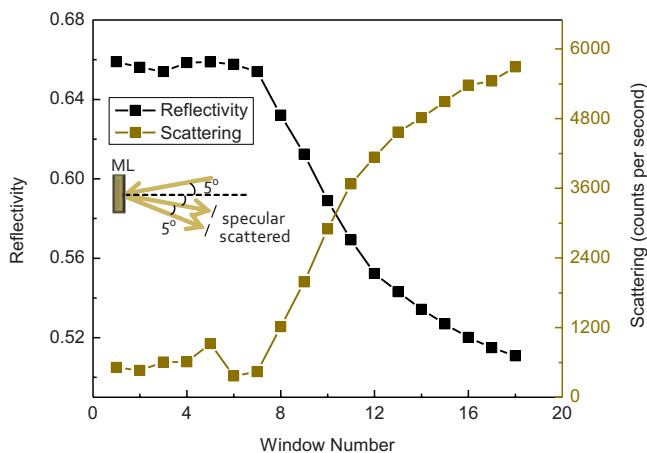
FIG. 5. (Color online) Reflectivity and scattering yields for the measurements from the different windows are shown on the scale of increasing roughness. Increase in scattering follows the decrease in reflectivity, indicating an increase in phase roughness. Wavelength of light used was 13.46 nm at a 5° angle of incidence for reflectivity relative to the normal. The scattering was obtained at a fixed angle that was 10° away from the normal.
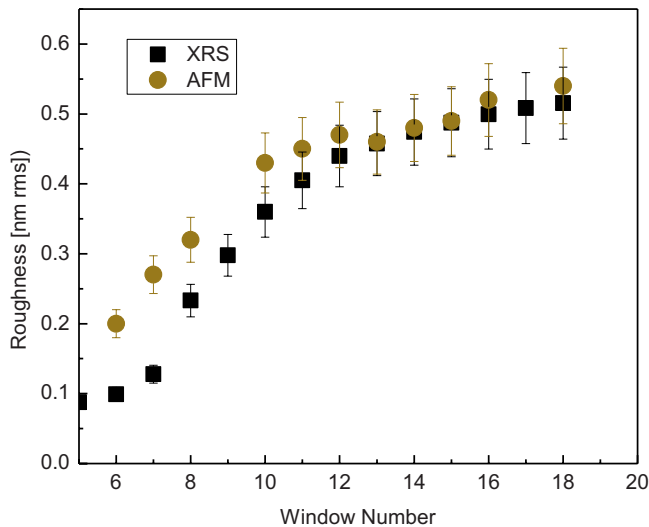
FIG. 6. (Color online) AFM and XRS measured rms roughness are compared. The two sets of data are seen to overlap where the substrate phase roughness heights are large and differ by nearly 50% for the low phase roughness mask areas. Fixed uncertainty at 10% is assumed for both sets of data as coming from the measurement errors.

In Fig. 6, the two sets of data are plotted for comparison against the region numbers. A fixed uncertainty of 10% is assumed for both measurements. The two sets of data in Fig. 6 are seen to overlap where the substrate phase roughness heights are large. In the smallest substrate roughness areas, XRS determined roughness is nearly 50% lower than the AFM measured roughness values.

III. ACTINIC MASK SURFACE IMAGING

The SEMATECH Berkeley Actinic Inspection Tool (AIT) is an EUV microscope used for mask inspection at an operating wavelength of 13.4 nm. Details of the system can be found in the literature.[24,25] In the imaging mode, the AIT operates as a high resolution, zone plate based EUV microscope designed to emulate EUVL stepper systems. Flare in the AIT is given to be 2%–3%,[24] the illumination partial coherence is found to be below 0.2, and the major aberrations in the system are shown to be astigmatism combined with focal plane tilt and coma.[25]

In the imaging mode, the zone plate projects a $907\times$ magnified image of the illuminated area on a mask onto a back illuminated, 1×1 in.[2], EUV charge coupled device (CCD) camera. A through-focus series of images for four different

regions at specific points along the rough gradient was collected with a 0.3 NA, $4\times$ stepper equivalent zone plate. Each image collected in the series is a 16 bit, 2048×2048 array corresponding to a 30 μm^2 area on the mask. An analysis of each image is completed to extract the appropriate speckle contrast in the image.

The full image area of the mask collected with the AIT CCD camera is not usable for analysis due to illumination nonuniformities and aberrations. The part of the image where the imaging can be considered diffraction limited is small compared to the overall image size and needs to be identified for each image. An analysis of each background corrected image area is completed by dividing the image into 256 arrays of 128×128 pixels that correspond to an area of 3.7 μm^2 on the mask. Each of these subarrays is then divided by its best fitting plane to correct for the illumination gradients and to normalize the data. For the rough mask surfaces imaged, the contrast of the granularities seen in the images is determined by computing the normalized standard deviations of the image intensities at the nearly diffraction limited area of each image.

Figure 7 gives an example of a typical series of through-focus images collected for a single multilayer window. The corresponding speckle contrast is also shown directly below each image in the series. For the rough mask surfaces imaged, the contrasts of the granularities seen in the images are determined to be a minimum at the best focus condition of the lens. The speckle contrast observed at the best focus of each set of data is plotted against the region number in Fig. 8. The adjacent table provides contrast data as well as the corresponding phase roughness determined from the AFM measurements. Even at the smallest roughness scale, a speckle contrast better than 6% is observed.

IV. SIMULATIONS

The question that is central to this article is: Can indirect top surface phase roughness characterizations be trusted explicitly for predicting scatter related speckle in the image field? In order to determine the accuracy of surface characterizations, we try to reproduce the image plane speckle determined from the AIT images by modeling the rms roughness content obtained with the AFM and XRS.

AIT imaging characteristics are modeled with a two dimensional (2D), scalar, aerial image computation software developed in-house. Scalar modeling and thin mask approxi-
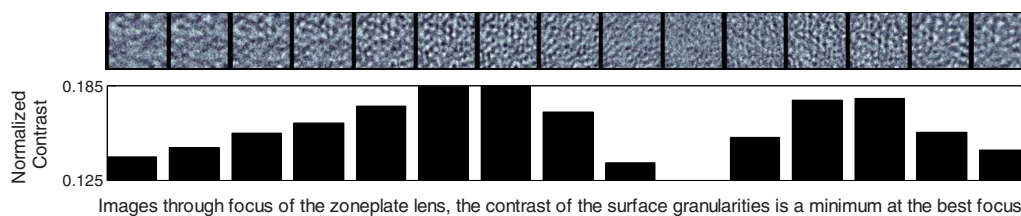

FIG. 7. (Color online) Image series through focus, collected for a single multilayer rough window using the AIT zone-plate EUV microscope. The corresponding speckle contrast, which is just the normalized standard deviation of the image intensities, is also shown for each image in the series. The minimum in focus is found for the tenth image from the left, where the granularities can be seen to be the smallest.

0.3 NA equivalent zone plate, FOV – 1 µm

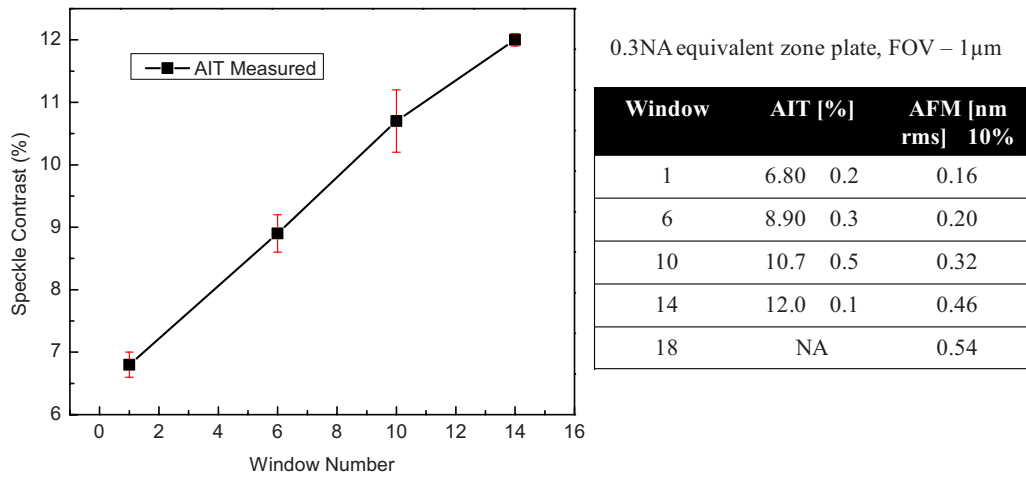| Window	AIT [%]		AFM [nm rms] 10%
1	6.80	0.2	0.16
6	8.90	0.3	0.20
10	10.7	0.5	0.32
14	12.0	0.1	0.46
18	NA		0.54

FIG. 8. Speckle contrast at the best focus of each rough surface through-focus datum collected is shown. The adjacent table provides contrast data as well as the corresponding phase roughness determined from the AFM measurements. Even at the smallest roughness scale, a speckle contrast better than 6% is observed.

mation are appropriate for the small NAs that are being used here.[9,26] The rough mask synthesized from the AFM image PSDs containing the phase error content is modeled as a pure phase distribution. The phase is determined from the geometric path length differences under the assumption that EUV light is reflected from the top surface of the mask.

Initial calculations were completed under the assumption that the AIT images are diffraction limited; this yielded speckle contrast values that were far from the AIT measured speckle. Subsequent calculations are completed including the AIT design aberrations. AIT design aberrations are computed for a 2 µm field using ray tracing methods and tabulated in Table III. Astigmatism and defocus are found to be the dominant Zernike terms in the system. Additionally, a 2.5% coherent optics produced scatter reported for the AIT is added in quadrature to the modeled speckle contrast at best focus.

The calculated speckle contrast based on the AFM measured roughness data is compared to the measured speckle, which is shown in Fig. 9. AIT image based contrast does not match completely to the calculated values, and a crossover point is observed near the high roughness regions. This is observed to be consistent through many simulation sets. When compared to XRS roughness data simulations, the

AFM is shown to be a better fit to the measured images. The plot of all data is given in Fig. 10, and the corresponding data points are tabulated in Table IV. All data are shown to overlap in the taller phase error conditions.

V. DISCUSSION

In this article, we try to systematically study the effects of substrate roughness on image plane speckle with the goal of determining adequate metrologies for RSR. Specifically, we considered AFM and X-ray reflectometry by predicting the speckle based on roughness measured using those techniques and then comparing it to direct AIT speckle measurements. The AFM and XRS based measurements of the rms phase roughness are observed to differ in the small roughness range that is characteristic of the EUV mask substrates fabricated at present. XRS calculated roughness based modeled data are shown to deviate further from the measured speckle contrasts in the small roughness regime. In the AIT measured to modeled speckle contrast comparison, AFM is shown to be better than the XRS, but it still fails to predict the measured speckle.

TABLE III. AIT design aberrations are computed for a 2 µm field using ray tracing. Astigmatism and defocus are found to be the dominant Zernike terms in the system.

|	Field location (x, y) µm									
Zernike numbers	0.0,0.0	0.0,0.5	0.0,1.0	0.5,0.0	0.5,0.5	0.5,1.0	1.0,0.0	1.0,0.5	1.0,1.0	Field-weighted average
Z3 (defocus)	−0.0017	−0.0161	−0.0305	−0.0017	−0.0161	−0.0304	−0.0016	−0.0160	−0.0303	−0.0189
Z4 (Astig. 90)	0.0012	0.0155	0.0297	0.0013	0.0156	0.0298	0.0014	0.0157	0.0299	0.0184
Z5 (Astig. 45)	0.0000	0.0000	0.0000	−0.0144	−0.0143	−0.0142	−0.0288	−0.0286	−0.0285	−0.0172
Z6 (Coma X)	0.0000	0.0000	0.0000	0.0040	0.0040	0.0040	0.0080	0.0080	0.0080	0.0048
Z7 (Coma Y)	0.0014	0.0052	0.0091	0.0014	0.0052	0.0091	0.0014	0.0052	0.0091	0.0060
Z8 (spherical)	−0.0002	−0.0002	−0.0001	−0.0002	−0.0002	−0.0001	−0.0002	−0.0002	−0.0001	−0.0002
Weight	1	2	2	2	4	4	2	4	4	
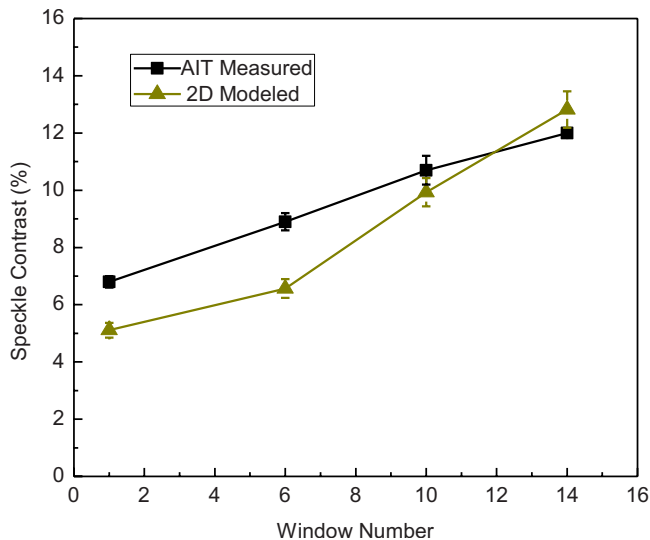
FIG. 9. (Color online) Calculated speckle contrast based on the AFM measured roughness data is compared to the measured speckle. AIT image based contrast does not match completely to the calculated values, and a crossover point is observed near the high roughness regions.

We attribute the XRS departure from the AFM measurements to two reasons. The first source of error is expected to be in the initial reflectivity chosen for XRS roughness calculations. It is an average of the reflectivities obtained for the first few rough surface regions in the very low roughness region. Ideally, we would want the initial reflectivity measurement to be free of any roughness at all, which in practice is not possible. The second major error comes from ignoring the absorption of the incident beam on the sample surface that could lead to the reflectivity loss. Not accounting for absorptive losses will drive the calculated rms roughness to be smaller as observed in the data here. For a better rough-
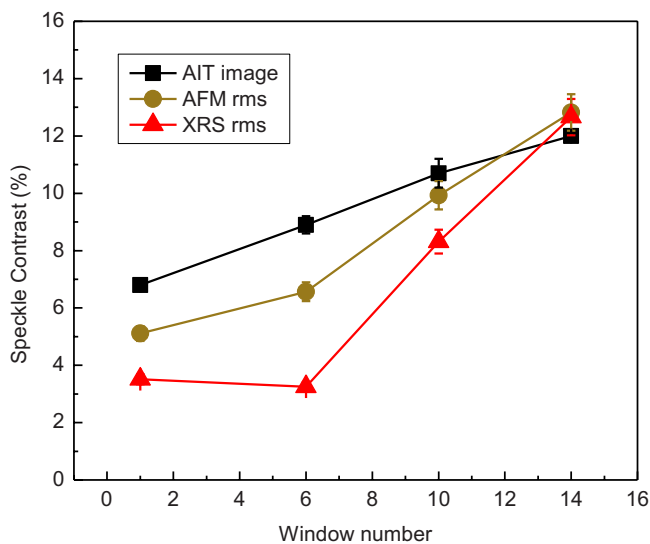

FIG. 10. (Color online) Calculated image contrast for AFM and XRS determined phase roughness compared to the measured image contrast. When compared to XRS roughness data simulations, the AFM is shown to be a better fit to the measured images. All data seem to overlap, within error, for the 0.5 nm rms roughness areas on mask.

TABLE IV. Comparing measured and simulated image speckle contrasts. Simulations are based on the rms roughnesses obtained from the AFM images and the XRS reflectance.

Window number	AIT measured speckle contrast (%)	2D modeled (AFM rms) speckle contrast (%)	2D modeled (XRS rms) speckle contrast (%)
1	6.8	5.1	3.5
6	8.9	6.6	3.2
10	10.7	9.9	8.3
14	12	12.8	12.7

ness metrology with XRS, we plan to measure the total integrated scatter and compare the scatter power spectral density information to the AFM image PSDs. We expect that the total integrated measurements will be a much more accurate method for determining the true roughness of the mask substrate since it serves as a direct measure of the scattered light, which is fundamentally what leads to the speckle. Further evaluations using resist exposures of the patterned rough areas with the SEMATECH Berkeley 0.3 NA micro-field exposure tool (MET) (Ref. 27) are being planned in order to better predict the impact of mask RSR on pattern LER.

Although, both AFM and XRS have the capability to characterize surfaces with rms height deviations in picometers, it is believed that the true nature of scattering arising from the multilayer interfaces that lie beneath the surface will not be evident from top surface only metrologies such as AFM. The data presented here suggest that neither AFM nor XRS (as implemented here) is an accurate measure of RSR. We do believe, however, that an improved scattering measurement can be employed that may alleviate the need to qualify mask blanks using image based mask speckle measurements. This is to be completed in the near future.

[1] R. H. Stulen and D. W. Sweeney, IEEE J. Quantum Electron. **35**, 694 (1999).
[2] V. Bakshi, *EUV Lithography* (SPIE, Washington, 2007).
[3] B. Wu and A. Kumar, *Extreme Ultraviolet Lithography* (McGraw-Hill, San Francisco, 2009).
[4] B. LaFontaine, A. R. Pawloski, Y. Deng, C. Chovino, L. Dieu, O. R. Wood II, and H. J. Levinson, Proc. SPIE **5374**, 300 (2004), and references therein.
[5] E. Spiller, *Soft X-Ray Optics* (SPIE Optical Engineering, Bellingham, WA, 1994), Vol. PM15.
[6] J. A. R. Samson and D. L. Ederer, *Vacuum Ultraviolet Spectroscopy* (Academic, San Diego, 1998), Vol. 1.
[7] D. Stearns and E. Gullikson, Physica B **283**, 84 (2000).
[8] D. G. Stearns, D. P. Gaines, D. W. Sweeney, and E. M. Gullikson, J.

Appl. Phys. **84**, 1003 (1998).

[9] J. W. Goodman, *Statistical Optics* (Wiley, New York, 1985).

[10] N. Beaudry and T. Milster, Opt. Lett. **25**, 454 (2000).

[11] International Technology Roadmap for Semiconductors, 2009 ed., http://www.itrs.net/

[12] R. Brainard, C. Henderson, J. Cobb, V. Rao, J. Mackevich, U. Okoroanyanwu, S. Gunn, J. Chambers, and S. Connolly, J. Vac. Sci. Technol. B **17**, 3384 (1999).

[13] G. Gallatin, Proc. SPIE **5754**, 38 (2005).

[14] P. P. Naulleau and G. Gallatin, J. Vac. Sci. Technol. B **26**, 1903 (2008), and references therein.

[15] P. P. Naulleau, D. Niakoula, and G. Zhang, J. Vac. Sci. Technol. B **26**, 1289 (2008).

[16] P. Naulleau, Appl. Opt. **48**, 3302 (2009).

[17] T. Liang *et al.*, J. Vac. Sci. Technol. B **25**, 2098 (2007).

[18] T. Pistor, T. Y. Deng, and A. Neureuther, J. Vac. Sci. Technol. B **18**, 2926

(2000).

[19] P. P. Naulleau and S. A. George, Proc. SPIE **7379**, 73790O (2009).

[20] P. P. Naulleau, S. A. George, and B. M. McClinton, Proc. SPIE **7636**, 76362H (2010).

[21] H. Kinoshita, T. Watanabe, A. Ozawa, and M. Niibe, Proc. SPIE **3412**, 358 (1998).

[22] SuMMIT Software Division of EUV Technology, Summit Litho Image Analysis Software, 2009, http://www.euvl.com/summit/

[23] E. M. Gullikson, S. Mrowka, and B. B. Kaufmann, Proc. SPIE **4343**, 363 (2001).

[24] K. A. Goldberg *et al.*, Proc. SPIE **6730**, 67305E (2007).

[25] K. A. Goldberg, I. Mochi, P. Naulleau, T. Liang, P.-Y. Yan, and S. Huh, J. Vac. Sci. Technol. B **27**, 2916 (2009), and references therein.

[26] E. Gullikson, C. Cerjan, D. Stearns, P. Mirkarimi, and D. Sweeney, J. Vac. Sci. Technol. B **20**, 81 (2002).

[27] P. P. Naulleau, Proc. SPIE **7636**, 76361J (2010).